Advanced Functional Materials

ADVANCED FUNCTIONAL MATERIALS
www.afm-journal.de

RESEARCH ARTICLE OPEN ACCESS

Magnetic Control of Chiral Hybridized Phonon Magnetic Moments in Ferrimagnets $Fe_{2-x}Zn_xMo_3O_8$

Youngsu Choi[1] | Dirk Wulferding[2] | Amit Pawbake[3] | Clément Faugeras[3] | Sivasakthi Kuppusamy[4] | Raman Sankar[4] | Gichan Son[5] | Jeongwoo Kim[5] | Kwang-Yong Choi[1]

[1]Department of Physics, Sungkyunkwan University, Suwon, Republic of Korea | [2]Department of Physics and Astronomy, Sejong University, Seoul, Republic of Korea | [3]Laboratoire National Des Champs Magnétiques Intenses, LNCMI-EMFL, CNRS UPR3228, INSA-T, Université Grenoble Alpes, University of Toulouse, Grenoble, France | [4]Institute of Physics, Academia Sinica, Taipei, Taiwan ROC | [5]Department of Physics, Incheon National University, Incheon, South Korea

Correspondence: Dirk Wulferding (d.wulferding@sejong.ac.kr) | Raman Sankar (sankarndf@gmail.com) | Kwang-Yong Choi (choisky99@skku.edu)

Received: 20 May 2025 | **Revised:** 28 April 2026 | **Accepted:** 28 April 2026

Keywords: chiral phonon | DFT calculations | phonon-magnon coupling | polar ferrimagnet

ABSTRACT

Chiral magneto-phononic modes—hybridized vibrational states that carry angular momentum through coupling with magnetic degrees of freedom—offer a novel route for controlling magnetism and enabling topological phononics. Here, we report the magnetic switching of these hybridized chiral phonons, $Zn_xFe_{2-x}Mo_3O_8$, using helicity-resolved magneto-Raman spectroscopy. By tuning the Zn concentration across antiferromagnetic and ferrimagnetic regimes, we uncover two key phenomena: (i) a giant, spontaneous zero-field splitting (~10 cm^{-1}) of the doubly degenerate E_2 hybridized phonon modes in the ferrimagnetic state, and (ii) a field-induced Zeeman effect in the antiferromagnetic and paramagnetic phases. The phonon splitting in the ferrimagnetic phase exhibits a pronounced asymmetry with respect to the applied field direction and shows a strong correlation with magnetization, highlighting a selective phonon-magnon coupling and the emergence of large effective magnetic moments driven by magnetization. Our results demonstrate that chiral hybridized phonons can be dynamically controlled through their intrinsic entanglement with magnon and spin degrees of freedom, enabling the tuning of effective magnetic moments via magnetization and external magnetic fields. These findings establish $Zn_xFe_{2-x}Mo_3O_8$ as a compelling platform for exploring novel magneto-phononic phenomena.

1 | Introduction

In solids, the angular momentum of electrons underlies a variety of Hall effects and topological phases. Analogously, the chirality of light provides a powerful means to manipulate electronic symmetries and induce chiral behavior through light-matter interactions. Recently, this chiral concept has been extended to phonons—the quantized vibrational modes of a crystal lattice [1–7]. Unlike conventional phonons, chiral phonons exhibit circular atomic displacements around their equilibrium positions and carry a pseudo-angular momentum even in the absence of an external magnetic field [8, 9]. This distinctive characteristic arises in materials that either lack inversion symmetry (i.e., chiral or non-centrosymmetric lattices) or break time-reversal symmetry. Singularly, chiral phonons feature a wide array of exotic phenomena, including the phonon Hall effect, phonon Einstein–de Haas effect, phonon Faraday effect, chiral-phonon-induced spin Seebeck effect, ultrafast demagnetization processes, and phonon Zeeman effect [10–32]. Beyond their fundamental significance, chiral phonons hold promise for dissipationless phononic circuits, opto-magnetic devices, topological phononics, advanced spintronic functionalities, and quantum information processing based on phononic degrees of freedom.

A key mechanism underpinning these emergent phenomena is the magnetization induced by circularly polarized light through the inverse Faraday effect, along with the magnetic control of chiral phonons. In the ionic angular momentum picture, the phonon magnetic moment is extremely small, typically on the order of the nuclear magneton ($\sim 10^{-5}$–10^{-3} μ_B) [8], since the ionic circular motion within a phonon mode generates only weak magnetic fields arising from its pseudo-angular momentum. By contrast, in the mode angular momentum picture, chiral phonons are treated as collective vibrational modes carrying quantized angular momentum along their propagation wavevectors. In conventional insulators, the phonon magnetic moment arises primarily from ionic motion and can be modestly enhanced through spin–phonon or orbit–phonon coupling, yet its value remains orders of magnitude below the Bohr magneton. However, strong magneto-phonon effects have been observed when chiral phonons are energetically proximate or entangled to electronic degrees of freedom, leading to a giant effective magnetic moment reaching up to about ~ 1 μ_B [23, 28, 33]. Theoretically, magnon-phonon hybridization, orbital-phonon resonance, and strong electron-phonon Berry curvature coupling in suitable symmetry and band structure [30–35] have been proposed as key mechanisms behind this enormous enhancement of hybridized phonon magnetic moments. As such, the measured magnetic moment is an ***effective*** quantity, reflecting the hybridization between the phonon's symmetry-dictated angular momentum and the electronic, magnetic, or spin environments.

In this context, polar magnetic compounds provide a prominent platform for the control of chiral hybridized phonons through magnetism, thanks to their inherent spin-lattice couplings as well as broken space-inversion and time-reversal symmetry. A recent study has uncovered a rich interplay between chiral phonons and spin fluctuations in the polar antiferromagnetic compound $Fe_2Mo_3O_8$ ($P6_3mc$ space group) [28]. The crystal structure of $Fe_2Mo_3O_8$ comprises alternating FeO_4 tetrahedral (Fe—I) and FeO_6 octahedral (Fe-II) units that form a honeycomb layer within the ab plane, separated by nonmagnetic Mo^{4+} layers, as shown in Figure 1a [36, 37]. Below the Néel temperature at T_N = 60 K, collinear antiferromagnetic (AFM) ordering takes place: within each Fe layer, the uncompensated magnetic moments align parallel to the *c* axis in a ferrimagnetic (FiM) arrangement, while adjacent layers couple antiferromagnetically, as illustrated by the spin configuration in Figure 1a [38–40]. As sketched in the temperature-field phase diagram of Figure 1b,c, the FiM state is achieved either by the application of a magnetic field along the *c*-axis or through Zn substitution in $Zn_xFe_{2-x}Mo_3O_8$ [38–43]. Notably, the proximity of the FiM phase to the AFM-paramagnetic phase boundary enhances spin fluctuations, which in turn hybridize with low-energy chiral phonons via symmetry-allowed magnetoelastic couplings. The pivotal role of chiral phonons and spin-phonon interactions is further evidenced by the observation of a huge thermal Hall effect and magnon polarons **[**44, 45**]**. By exploiting the tunability of the AFM–FiM phase transition through Zn substitution, Zn-substituted $Fe_2Mo_3O_8$ offers valuable insight into the magnetic control of phonon chirality.

In this paper, we investigate chiral phonon behavior across different magnetic ordering regimes in $Zn_xFe_{2-x}Mo_3O_8$ using helicity-resolved magneto-Raman spectroscopy. Our composition-, field-, and temperature-dependent measurements reveal a giant spontaneous frequency splitting of hybridized phonon modes below the FiM temperature, even at zero field, in addition to the conventional phonon Zeeman effect in the AFM and paramagnetic states. The strong correlation between the enhanced energy splitting between left- and right-circular phonons and the magnetization showcases the tunable nature of chiral hybridized phonons through the control of spontaneous magnetization in this system.

2 | Results

We first examine the magnetic properties of $Zn_xFe_{2-x}Mo_3O_8$ for compositions x = 0.05, 0.24, and 0.35. For the slightly Zn-substituted sample (x = 0.05), the temperature dependence of the magnetic susceptibility measured under an applied field of $\mu_0 H$ = 0.5 T//c shows a sharp peak at $T_N \approx 58$ K, characteristic of the Néel ordering, see Figure 1d. The magnetization curves $M(H)$ for selected temperatures below T_N are displayed in Figure 1g. The overall magnetic behavior is comparable to that of the pristine sample (see Figure S1). Specifically, at T = 50 K, $M(H)$ features a two-step increase with increasing magnetic field, indicative of a magnetic transition from the AFM to the FiM state, with the corresponding critical fields shifting to higher fields as the temperature is lowered.

Upon further Zn substitution (x = 0.24 and 0.35), the temperature dependence of M/H shows a steep increase near $T_C \approx 51$ and 48 K, respectively, followed by saturation at lower temperatures, see Figure 1e,f, respectively. As exhibited in Figure 1h, the $M(H)$ curve of x = 0.24 features an *S*-shape behavior with negligible remanent magnetization below T_C. At temperatures below 30 K, a hysteretic behavior appears, characterized by a nonzero remanent magnetization corresponding to a FiM configuration, accompanied by a broadening of the hysteresis loop. A spontaneous magnetization and coercivity in the magnetization loops are also observed for x = 0.35, as displayed in Figure 1i. With increasing the Zn content from x = 0.24 to 0.35, the saturation magnetization is enhanced, while the hysteresis width slightly decreases. It is because as Zn progressively substitutes for Fe—I (tetrahedral site: orange balls and arrows in Figure 1a), the net magnetic moment at the tetrahedral sublattice is reduced, while the octahedral Fe-II moments remain largely unaffected. Such selective dilution weakens the interlayer AFM coupling and facilitates FiM alignment between layers since the magnetic moments of the tetrahedral and octahedral sublattices become increasingly unequal [41, 42]. This enhanced imbalance between the two sublattice moments yields a larger net magnetization at higher Zn content. Concurrently, the substitution of non-magnetic ions at the Fe1 site effectively reduces spin stiffness and long-range magnetic rigidity. Notably, the non-magnetic concentration in the x = 0.35 sample exceeds the site percolation threshold for a honeycomb lattice ($p_c \approx 0.697$) [46]. In a strictly 2D system, such a concentration is expected to cause the collapse of long-range magnetic order. While finite interplane coupling prevents the complete disruption of ferrimagnetic ordering, the long-range order is significantly destabilized. This provides a rationale for the observed trends in the x = 0.35 sample, specifically the reduction in T_C, the softer magnetic response, and the lack of magnetic stiffness, compared to the x = 0.24 composition. We

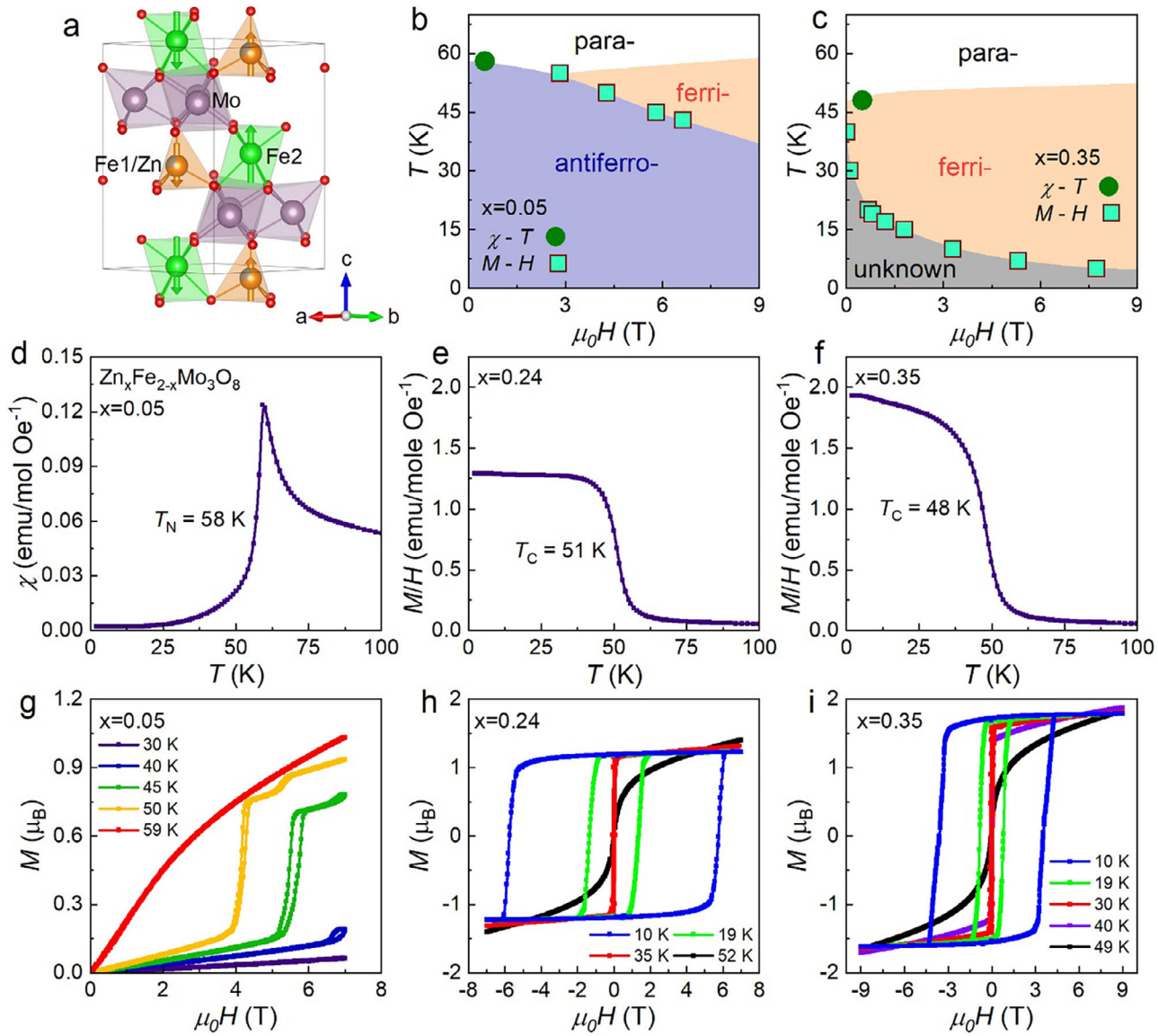

FIGURE 1 | a) crystal structure of $Fe_{2-x}Zn_xMo_3O_8$. The orange and green balls represent Fe1/Zn and Fe2 atoms, respectively, while the purple balls denote Mo atoms. The arrows represent the magnetic moment directions of Fe atoms. Temperature-field phase diagrams for b) $x = 0.05$ and c) $x = 0.35$, showing transitions between paramagnetic, antiferromagnetic, ferrimagnetic, and unknown magnetic phases. Temperature dependence of magnetic susceptibility for d) $x = 0.05$ along the *c*-axis under $\mu_0 H = 0.5$ T (zero-field cooled) and M/H for e) $x = 0.24$ and f) 0.35 (field cooled), indicating antiferromagnetic and ferrimagnetic transition temperatures T_N and T_C. g–i) Isotherm magnetization curves measured along the *c*-axis at selected temperatures for $x = 0.05$, 0.24, and 0.35, demonstrating the evolution of hysteresis behavior.

further stress that the combined X-ray diffraction and X-band ESR data effectively preclude the existence of phase separation or secondary impurities, providing evidence for the structural uniformity and chemical homogeneity of the $Zn_xFe_{2-x}Mo_3O_8$ series (see Figures S2 and S3).

Figure 2a presents the unpolarized Raman spectra collected at $T = 23$ K for compositions with $x = 0.0$, 0.05, 0.24, and 0.35 (see Figures S4–S6 for full Raman spectra and factor group analysis). All samples exhibit a series of sharp phonon modes that progressively soften and broaden across the AFM-to-FiM transition. A particularly notable feature is the evolution of the low-frequency $E_2(1)$ phonon mode near 50 cm^{-1}, which displays a distinct splitting for $x = 0.24$ and 0.35. Since only a single peak is observed in the AFM samples ($x = 0$ and 0.05), the splitting cannot be attributed to magnetic unit cell doubling and lattice distortions. In sharp contrast, the high-frequency $E_2(10)$ modes near 330 cm^{-1} show the double-peak feature across all studied compounds. In the paramagnetic phase, the doubly degenerate E_2 modes are protected by time-reversal symmetry (TRS) together with the crystal symmetries. Upon entering the FiM phase, spontaneous breaking of TRS can lift this protection. If phonons are endowed with chirality (see Figure 3), the internal FiM Weiss field acts like an effective magnetic field, leading to a zero-field phonon splitting with opposite angular momentum. This phonon Zeeman effect vanishes in the AFM state, where sublattice magnetizations cancel, explaining the composition-dependent behavior of the $E_2(1)$ phonon mode. In sharp contrast, the $E_2(10)$ phonon mode shows a pronounced zero-field splitting already in the AFM phase, indicating that its origin is not solely due

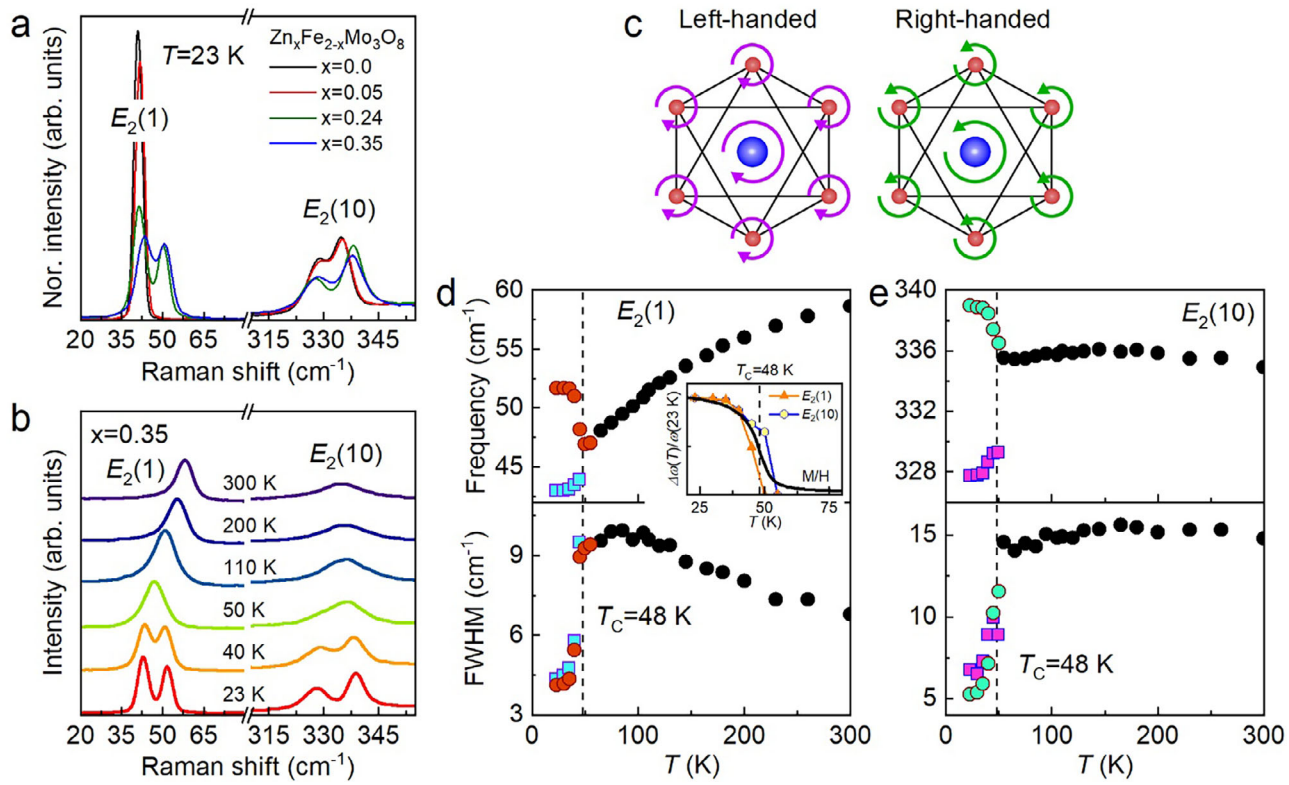

FIGURE 2 | a) Unpolarized Raman spectra of $Fe_{2-x}Zn_xMo_3O_8$ ($x = 0.0$, 0.05, 0.24, and 0.35) measured at $T = 23$ K, focusing on the low-energy $E_2(1)$ phonon and the high-energy $E_2(10)$ phonon mode. b) Temperature dependence of the $E_2(1)$ and $E_2(10)$ phonon modes for $x = 0.35$ measured at $T = 23$ - 300 K. c) Schematic of the atomic displacements of $E_2(1)$ phonons (Mo and O atoms) based on DFT calculations. d, e) Thermal evolution of the frequency and the full-width at half-maximum (FWHM) of $E_2(1)$ and $E_2(10)$ in $x = 0.35$. The doubly degenerate E_2 modes undergo splitting in the magnetically ordered state (marked by the vertical dashed lines). The inset plots the temperature dependence of $E_2(1)$ and $E_2(10)$ phonon splitting below T_C. The M/H curve (solid line) closely follows the thermal evolution of the phonon frequencies below T_C. The linewidths drastically narrow on cooling through T_C.

to TRS breaking. Instead, this behavior suggests that the E2(10) mode couples more strongly to anisotropic spin correlations or bond-dependent modulations of exchange paths, which can effectively lower the lattice symmetry even in the absence of a net magnetization. As a result, the degeneracy of this mode can be lifted in both AFM and FiM phases. These observations highlight the mode-selective nature of spin–phonon coupling and its sensitivity to the underlying magnetic symmetry and exchange pathways.

Shown in Figure 2b are the temperature-dependent Raman spectra for $x = 0.35$, focusing on the thermal evolution of the $E_2(1)$ and $E_2(10)$ modes. As the temperature decreases from 300 to 23 K, most phonon modes sharpen and shift to higher frequencies, consistent with conventional anharmonic effects. Notably, the $E_2(1)$ phonon mode shows significant anomalies near the FiM transition temperature, $T_C = 48$ K (see Figure 2c and Figure S8 for the normal mode displacement of the $E_2(1)$ phonon). Figure 2d,e displays the temperature evolution of the frequencies and the full-width at half-maximum (FWHMs) of the $E_2(1)$ and $E_2(10)$ modes for $x = 0.35$. The $E_2(1)$ mode softens by approximately 10 cm^{-1} as the temperature is lowered toward T_C. Such a renormalization of the phonon self-energy is also observed in the pristine sample and is ascribed to strong spin-phonon coupling (see Figure S5 and Ref. 28). Below T_C, the mode splits by about 10 cm^{-1}, and the frequency difference between the split components exhibits a strong correlation with the M/H data (thick solid line), see the inset of Figure 2d. This order-parameter-like behavior highlights that the chiral phonon splitting is predominantly driven by internal FiM Weiss fields, as further evidenced by the helicity-resolved measurements presented in Figure 3. We note that the $E_2(1)$ phonon mode acquires magnetic moments through its hybridization with magnons revealed by magnon polarons, demonstrating its hybrid character [45]. In the same vein, the FWHM increases with decreasing temperature to T_C , thereby deviating markedly from the expected narrowing behavior based on lattice anharmonicity. Below T_C , the linewidth decreases substantially. This anomalous trend further supports that the lifetime of the $E_2(1)$ hybridized phonon is dictated by magnetic fluctuations rather than lattice anharmonicities. More specifically, the $E_2(1)$ hybridized phonon broadens on approaching T_C due to enhanced critical fluctuations. Below T_C, we observe the spontaneous splitting of the $E_2(10)$ mode, amounting to approximately 10 cm^{-1}, in conjunction with the line narrowing. In contrast to the $E_2(1)$ chiral phonon, however, the frequency and FWHM of the $E_2(10)$ mode show little variation with temperature in the paramagnetic state. This behavior is attributed to the fact that the $E_2(10)$ mode lies far above the magnon energy (see M mode in Figure 3a), resulting in negligible phonon-magnon coupling.

Figure 3 shows the magnetic field dependence of the chiral hybridized phonon $E_2(1)$ and the magnon mode M (113 cm^{-1}), measured at $T = 2$ K using two cross-circular scattering

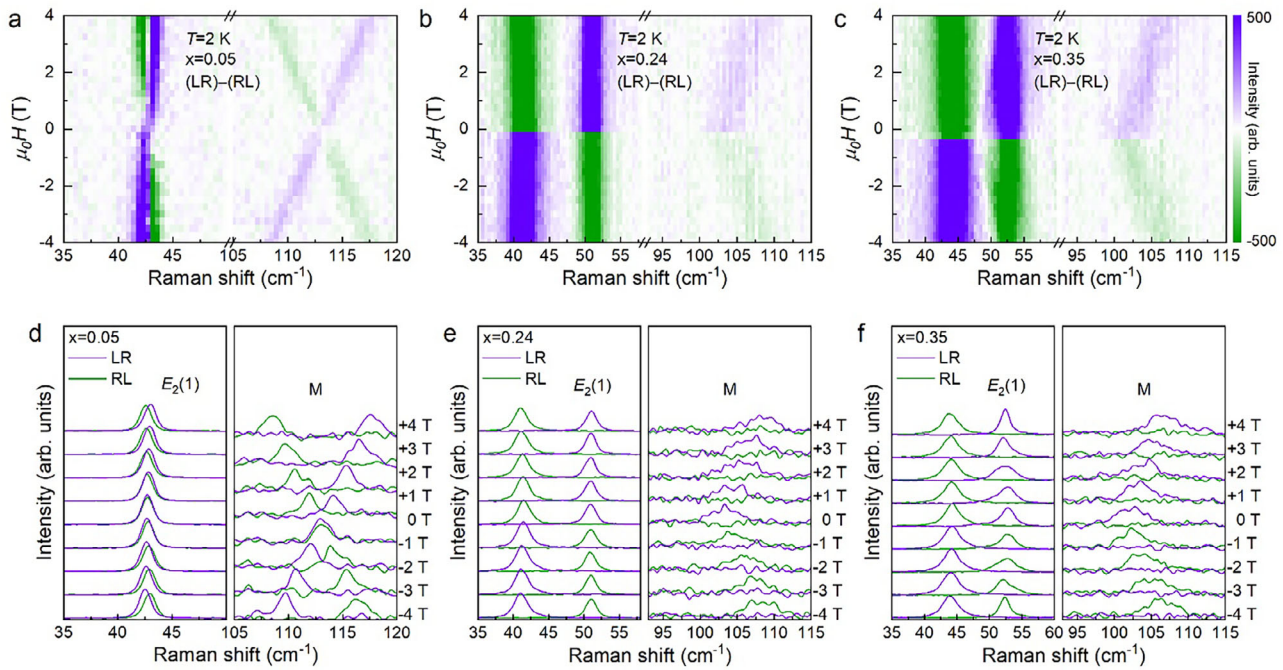

FIGURE 3 | Color plot of the Raman dichroism, defined as the differential intensity I_{LR}-I_{RL}, where I_{LR} corresponds to left-circularly polarized incident light with right-circularly polarized detection (shown in purple) and I_{RL} to right-circularly polarized incident light with left-circularly polarized detection (shown in green), as a function of magnetic field and Raman shift. The Raman dichroism for the selected $E_2(1)$ phonon at 42 cm^{-1} and magnon mode at 112 cm^{-1} is measured for a) $x = 0.05$, b) 0.24, and c) 0.35 in the field range of $\mu_0 H = 4$ to −4 T at 2 K. The corresponding Raman spectra of the chiral $E_2(1)$ phonon (left panels) and magnon mode M (right panels) are plotted for d) $x = 0.05$, e) 0.24, and f) 0.35 under LR and RL polarization channels at $T = 2$ K over the field range of −4 T to 4 T.

configurations for compositions $x = 0.05$, 0.24, and 0.35. The full Raman spectra are presented in Figures S9–S11. The purple and green peaks correspond to left-handed circular excitation with right-handed emission (*LR*), and right-handed excitation with left-handed emission (*RL*), respectively. The circular dichroism is defined as (I_{LR}-I_{RL}), which quantifies the difference in Raman scattering intensities between the left- and right-circularly polarized light. In the Stokes-Raman processes, chiral phonons obey the conservation of pseudospin angular momentum (PAM) in addition to the conventional energy and momentum conservation: $\sigma_i - \sigma_s = m_{ph}$ (mod N), where σ_i (σ_s) denotes the angular momenta of the incident (scattered) photon, and m_{ph} is the PAM of the phonon. Given that the six-fold rotational symmetry of $(Zn_xFe_{1-x})_2Mo_3O_8$ is reduced to a three-fold symmetry in the AFM order, $N = 3$. As a consequence, the incident ($\pm\hbar$) and scattered photons ($\mp\hbar$) carry opposite angular momenta, so $m_{ph} = \mp 2\hbar$ (mod 3). These helicity-dependent selection rules dictating photon-phonon interactions are consistent with the behavior of the $E_2(1)$ hybridized phonon, thereby confirming the PAM conservation. We note that the phonon angular momentum is not directly determined by the PAM. To verify the chiral character of the phonons, we computed the z component of their angular momentum L_z (see Figure S7). The results show that the E modes possess finite angular momenta near the Γ point, while the $E_2(1)$ phonon displays significant energy deviation arising from strong phonon–magnon coupling due to their close energy proximity. Such a coupling will lead to a renormalization of the phonon energy and induce an in-phase rotation of the phonon and magnon normal modes.

For $x = 0.05$, we observe a linear Zeeman splitting of the doubly degenerate $E_2(1)$ hybridized phonon modes and AFM magnons with increasing magnetic field. Notably, the field-induced splittings of the hybridized phonon and magnon modes exhibit opposite circular polarizations, indicating that they carry angular momenta of opposite signs under magnetic fields. A similar trend has been reported in pristine $Fe_2Mo_3O_8$ [28]. From the slopes of the frequency shifts of the chiral hybridized modes with respect to the applied magnetic field, we estimate their effective magnetic moments using the low-field linear relation $.\mu_{pm} = \frac{1}{2}\frac{\partial(\omega_R - \omega_L)}{\partial(\mu_0 H)}]_{H\to 0}$ where ω_R and ω_L are the frequencies of the right- and left-handed circularly polarized phonons (see Figure S12). We obtain the effective magnetic moments of $\mu_{pm} = 0.11\ \mu_B$ per mode for the $E_2(1)$ chiral hybridized mode and $\mu_{mag} = 2.24\ \mu_B$ per Fe for the magnon. Here, we note that the $E_2(1)$ mode represents a hybrid excitation rather than a pure phonon. As such, the large effective moments should not be regarded as phonon-only magnetic moments. Instead, they stem from strong magnetoelastic hybridization, as evidenced by the nonlinear Zeeman response in the FiM sample, which reflects the dominant influence of the underlying magnetic state. In the regime of strong magnetoelastic coupling, phonon and magnon degrees of freedom are entangled.

Among the proposed mechanisms, phonon-magnon hybridization is particularly relevant to our multiferroic system [28]. In this scenario, direct coupling between optical phonons and magnons allows their wavefunctions to mix, endowing the hybrid

mode with an effective magnetic moment μ_{pm} proportional to its magnon component: $\mu_{pm} \approx (\gamma/\Delta)^2 \mu_{mag}$ where γ denotes the magnon-phonon coupling strength, and Δ is the energy mismatch between the two modes.

Based on the experimentally obtained values, we deduce $\gamma/\Delta \sim 0.22$. The resulting moderate hybridization of the magnon component in the chiral phonon is in qualitative agreement with neutron scattering results [45], thereby supporting our analysis. Notably, other mechanisms such as orbital-phonon coupling observed in monolayer MoS_2 or resonant electron-phonon coupling in topological and Dirac materials [33] appear less relevant for the studied compounds, as discussed further below.

For $x = 0.24$ and 0.35 (FiM phase), the $E_2(1)$ hybridized mode undergoes a giant spontaneous frequency splitting of 11 cm^{-1} at zero magnetic field—approximately 25% of the phonon frequency. The right- and left-circularly polarized components display little variation with applied fields, indicating the negligible phonon Zeeman effect. Such spontaneous splitting of chiral hybridized phonons due to intrinsic bulk magnetization, in the absence of an external magnetic field, has also been reported in the ferromagnetic Weyl semimetal $Co_3Sn_2S_2$ [47]. However, the splitting (1.27 cm^{-1}) is nearly an order of magnitude smaller than that observed in ferrimagnetic $Fe_{2-x}Zn_xMo_3O_8$. We further note that the FiM magnon with left-handed circular polarization predominantly emerges under positive magnetic fields, whereas the right-circularly polarized magnon becomes prominent when the external field is reversed. The selectivity of FiM magnon chirality arises from the orientation of the FiM domain (the sign of the net angular momentum), which can be controlled by the magnetic field direction.

Figure 4a,b maps the magnetic field dependence of the Raman circular dichroism for the chiral hybridized phonons $E_2(1)$ and $E_2(10)$ at $T = 4.2$ K (below T_C) and $T = 65$ K (above T_C) for $x = 0.35$. In the paramagnetic state, both $E_2(1)$ and $E_2(10)$ phonons exhibit Zeeman splitting with opposite polarizations. Well below T_C, a large energy splitting of ~ 10 cm^{-1} is observed for the chiral $E_2(1)$ and $E_2(10)$ hybridized phonons, attributed to spontaneous time-reversal symmetry breaking at zero field. In Figure 4c,d, we plot the field evolution of the peak frequencies of the $E_2(1)$ and $E_2(10)$ hybridized phonons at selected temperatures. To elucidate the underlying mechanism of chiral phonon splitting, the extracted frequency-field behavior is directly compared with the corresponding magnetization curves. Evidently, the phonon splitting changes sign when the magnetization direction reverses under the application of a magnetic field along the *c* axis. At $T = 65$ K (above T_C), the hybridized phonon Zeeman splitting exhibits a nearly linear dependence on the applied magnetic field, closely tracking the $M(H)$ curve. Near the critical temperature, the hybridized phonon Zeeman shift continues to follow the magnetization behavior. At $T = 20$ K, where the hysteresis loop becomes apparent (see Figure 1i), the $E_2(1)$ hybridized mode displays a spontaneous zero-field splitting that emulates the $M(H)$ behavior. A closer inspection reveals that the left-circularly polarized branch remains nearly field-independent, while the right-circularly polarized branch exhibits a notable linear increase with increasing magnetic field. Notably, this asymmetric Zeeman response is hardly discernible for the higher-frequency $E_2(10)$ phonon mode. As such, the formation of hybridized magnon polarons should be invoked as an underlying mechanism [47, 48]. Indeed, such magnon–polaron states have been reported in related systems, including $Fe_2Mo_3O_8$ [45] and Zn-substituted $Fe_{1.75}Zn_{0.25}Mo_3O_8$ [49, 50], where switching of chiral phonons is observed in tandem with magnetization, along with momentum-resolved detection of chiral phonons carrying substantial magnetic moments.

Specifically, the $E_2(1)$ chiral hybridized phonon is resonant with magnon excitations, which explains its pronounced field sensitivity compared to the higher-frequency $E_2(10)$ chiral phonon. Moreover, this coupling is chiral-selective: only the left-circularly polarized phonon interacts with the FiM magnon under a positive magnetic field, while the right-circularly polarized phonon couples when the field (thus the magnetic moment) is reversed [30]. This selective magnon-phonon interaction underlies the asymmetric Zeeman response observed in the $E_2(1)$ hybridized mode.

The linear relationship between the chiral phonon splitting and magnetization observed below T_C provides compelling evidence for its correlation with magnetization. Within the framework of spin-phonon coupling, the splitting of the doubly degenerate E_2 hybridized modes is linearly proportional to magnetization, expressed as $\Delta\omega_m \sim \gamma_m M(T, H)$ with the phonon-magnetization coupling constant γ_m. In certain conditions, this magnetization-induced splitting can be significantly larger than the field-induced splitting $\Delta\omega_H \sim \gamma_H H$ [28]. Taken together, the chiral hybridized phonons in $(Zn_xFe_{1-x})_2Mo_3O_8$ acquire their angular momentum primarily through spin-phonon coupling and magnon–phonon hybridization. We further consider several alternative mechanisms that could explain the anomalous features of the $E_2(1)$ hybridized phonon mode. Dynamic mode mixing is unlikely to play a major role, given the absence of soft phonon modes associated with the multiferroelectric transition and the lack of evidence for strong anharmonicity. Likewise, exciton–phonon coupling mediated by Berry curvature or hybridization with low-lying crystal field excitations can be excluded, as $(Zn_xFe_{1-x})_2Mo_3O_8$ exhibits a sizable band gap of approximately 1.1 eV, substantially larger than the $E_2(1)$ phonon energy, and the incident photon energy (~2.3 eV) lies far off resonance with any low-energy electronic excitations. On the other hand, dynamic coupling between lattice vibrations and magnetoelectric order parameters remains relevant in multiferroics and polar magnets. Such coupling can admix phonon angular momentum into magnetic or electric excitations, thereby enabling chiral hybridized phonons to exchange angular momentum with magnetic moments and influence magnetoelectric responses.

Lastly, we stress that the $E_2(1)$ hybridized mode in $(Zn_xFe_{1-x})_2Mo_3O_8$, arising from moderate magnon-phonon coupled excitations, enables coherent phase-locking of the coupled modes. However, slight off-resonant magnon-phonon coupling prevents detecting avoided crossings, unlike in $FePSe_3$ [51], in which magnon polarons emerge clearly under tunable experimental conditions, exhibiting strong hybridization consistent with theoretical models of anisotropic magnetoelastic interactions. Achieving a resonant magnon-phonon coupling regime in $(Zn_xFe_{1-x})_2Mo_3O_8$ would therefore require tuning

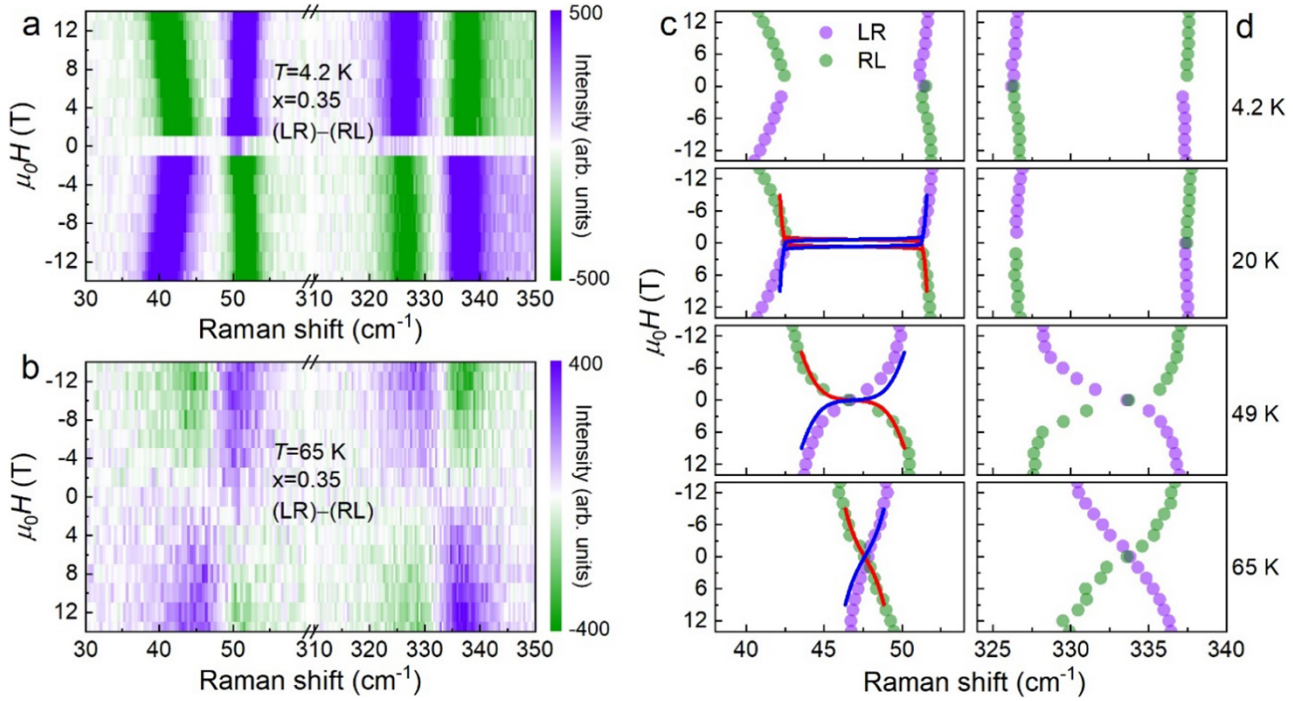

FIGURE 4 | Color plots of the Raman dichroism $I_{LR}-I_{RL}$ of chiral phonons $E_2(1)$ and $E_2(10)$ of $x = 0.35$ measured at a) $T = 4.2$ K and b) $T = 65$ K over magnetic fields up to ±14 T. Chiral phonon features show pronounced field-induced splitting at low temperatures. Field-dependent peak positions extracted from *LR* (purple) and *RL* (green) polarization channels at representative temperatures ($T = 4.2$, 20, 49, and 65 K), showing the evolution of Zeeman splitting in c) the low-frequency chiral $E_2(1)$ phonon and d) the high-frequency $E_2(10)$ mode. Colored lines in c) represent magnetization curves overlaid to demonstrate the correlation between phonon splitting and magnetization.

phonon or magnon energies through hydrostatic pressure or high magnetic fields. Given the $P6_3mc$ space group with E_g symmetric phonons, distinct from those of $FePSe_3$, our system provides a promising avenue for exploring newly emergent aspects in magneto-phononics.

3 | Conclusion

In conclusion, we have demonstrated magnetic switching of chiral hybridized phonons in ferrimagnets $(Zn_xFe_{1-x})_2Mo_3O_8$ through a comprehensive study of field- and temperature- and helicity-dependent Raman spectra. In the ferrimagnetic state, the $E_2(1)$ and $E_2(10)$ hybridized phonons exhibit large spontaneous zero-field splittings due to broken time-reversal symmetry, with their frequency shifts closely emulating the magnetization. The chiral phonon–magnon resonance leads to selective coupling with circularly polarized phonons, resulting in asymmetric Zeeman responses of the $E_2(1)$ chiral hybridized phonon. In contrast, the paramagnetic and antiferromagnetic phases exhibit linear Zeeman effects consistent with conventional spin-phonon coupling. The comparative study of chiral hybridized phonons across diverse magnetic phases in the $(Zn_xFe_{1-x})_2Mo_3O_8$ family demonstrates the efficient control of chiral magneto-phononic properties through the manipulation of distinct magnetic orders and magnetization states. Our findings establish polar ferrimagnets like $(Zn_xFe_{1-x})_2Mo_3O_8$ as exceptional platforms for the development of next-generation hybrid phononic and spintronic technologies.

4 | Experimental Section/Methods

4.1 | Sample Synthesis

$Fe_2Mo_3O_8$ and Zn-substituted $Fe_2Mo_3O_8$ single crystals were grown using the chemical vapor transport (CVT) method, which utilized a temperature gradient to facilitate controlled mass transport. High-purity Fe_2O_3, MoO_3, ZnO, Fe, and Zn powders were weighed in stoichiometric ratios, thoroughly ground using an agate mortar and pestle, and sealed in an evacuated quartz ampoule. The precursor materials were pre-reacted at 750°C and 1000°C for two days. Approximately 10 g of the pre-reacted $Fe_2Mo_3O_8$ and Zn-substituted powder, along with 120 mg of $TeCl_4$ (4N purity) as the transport agent, was placed at one end of a silica ampoule (40 cm in length, 1.8 cm inner diameter, and 2.0 cm outer diameter). The chlorine concentration of 3.6–4.7 mg, derived from ~5 mg of $TeCl_4$ per cm^3, yielded sufficient transport rates of nearly 150 mg per day. All preparation steps before flame sealing were conducted in an argon-filled glovebox, ensuring oxygen and moisture levels remained below ~1 ppm.

For the growth of $Fe_2Mo_3O_8$ and Zn-substituted $Fe_2Mo_3O_8$ single crystals, the end of the ampoule containing the pre-reacted material was held at 950°C, while the growth end was maintained at approximately 900°C, creating a temperature gradient of about 2.5°C/cm for a week. The material was then loaded into a quartz ampoule along with 5–10 mg/cm^3 of iodine (I_2) or $TeCl_4$ as the transport agent. The ampoule was subsequently evacuated to ~10^{-6} Torr and flame-sealed under vacuum before being placed

in a two-zone furnace. The source zone was maintained at ~950°C, while the growth zone was set at ~900°C, ensuring a temperature gradient of 100°C for 7–14 days. After crystal growth, the furnace was slowly cooled to room temperature to minimize thermal stress. The ampoule was then opened in an inert atmosphere (e.g., an Ar-filled glovebox) to prevent oxidation. The extracted $Fe_2Mo_3O_8$ single crystals were cleaned using ethanol or a dilute acid solution (e.g., HCl or HNO_3) and dried before characterization.

4.2 | Magnetization and Magnetic Susceptibility

DC magnetic susceptibility and the isothermal magnetization measurements were performed using the vibrating sample magnetometer (VSM) option of a Superconducting Quantum Interference Device (SQUID) magnetometer (Quantum Design MPMS) and a Physical Property Measurement System (PPMS Dynacool, Quantum Design). The measurements were performed over a temperature range of $T = 2$–300 K, with the external magnetic field applied parallel to the crystallographic c-axis ($\mu_0 H \parallel c$) of the single-crystal samples.

4.3 | Raman Spectroscopy

Temperature-dependent Raman scattering experiments were conducted in a backscattering geometry using a diode-pumped solid-state single-longitudinal-mode (DPSS SLM) laser with an excitation wavelength of $\lambda = 532$ nm. The laser beam, operated at a power of 100 μW, was focused onto the crystal surface using a 40 × magnification microscope objective, yielding a spot size of a few micrometers. The scattered light was collected using a micro-Raman spectrometer (XperRam200VN, Nanobase) equipped with an air-cooled charge-coupled device (CCD) camera (Andor iVac). To suppress Rayleigh scattering, a notch filter with a low-frequency cutoff of 20 cm^{-1} was employed. Temperature control over the range of 5–300 K was achieved using a liquid-helium-cooled continuous-flow cryostat. Raman spectroscopic measurements in high magnetic fields up to 14 T were conducted at LNCMI Grenoble using a custom-built magneto-optical Raman probe [52] mounted inside a superconducting magnet (Oxford Instruments). A 515 nm laser (Azurlight Systems) was used for excitation, with the laser power kept below 0.3 mW and a focused spot size of approximately 3 μm at the sample position. Additional measurements with finer magnetic field resolution (up to 4 T) were performed using a closed-cycle Oxford Spectromag system. In this setup, light from a 660 nm laser (Cobolt), with a power of less than 4 mW, was focused through a set of lenses to yield a spot diameter of ~100 μm. In both configurations, the Raman-scattered light was dispersed using the single-stage TriVista spectrometer (Princeton Instruments) and detected by a nitrogen-cooled CCD camera (PyLoN eXcelon), following rejection of Rayleigh scattering via a set of customized Bragg-grating filters (OptiGrate).

4.4 | DFT Calculations

Density functional theory (DFT) calculations were performed using the projector augmented-wave (PAW) method [53, 54], as implemented in the Vienna Ab Initio Simulation Package (VASP) [55]. The exchange–correlation functional was treated within the generalized gradient approximation (GGA) using the Perdew–Burke–Ernzerhof (PBE) formulation [56]. The self-consistent field (SCF) iterations were converged to an energy threshold of 10^{-7} eV, and a plane-wave energy cutoff of 500 eV was employed. The Brillouin zone was sampled using a dense 12 × 12 × 6 Monkhorst-Pack k-point mesh. Structural relaxations were carried out until the residual forces on all atoms were less than 0.001 eV/Å. Phonon dispersion relations were calculated using the Phonopy package [57, 58] in conjunction with VASP, utilizing a 2 × 2 × 1 supercell for finite displacement calculations. Spin–orbit coupling (SOC) effects were not included in the present study.

Acknowledgements

KYC is supported by the National Research Foundation (NRF) of Korea (Grants No. 2020R1A2C3012367 and No. 2020R1A5A1016518). This research was supported by the Nano-Material Technology Development Program through the National Research Foundation of Korea (NRF) funded by the Ministry of Science and ICT (RS-2023-00281839). YC is supported by the National Research Foundation (NRF) of Korea (Grants No. RS-2023-00214312). D.W. acknowledges support from the Institute of Applied Physics of Seoul National University, from the ITRC Program through the IITP, and from the Global Research Development Center (GRDC) Cooperative Hub Program through the NRF, funded by the (MSIT) (Grant Nos. RS-2024-00437191 and RS-2023-00258359).

Conflicts of Interest

The authors declare no conflicts of interest.

Data Availability Statement

The data that support the findings of this study are available from the corresponding author upon reasonable request.

References

1. A. G. McLellan, "Angular Momentum States for Phonons and a Rotationally Invariant Development of Lattice Dynamics," *Journal of Physics C: Solid State Physics* 21 (1988): 1177–1190, https://doi.org/10.1088/0022-3719/21/7/009.

2. L. Zhang and Q. Niu, "Angular Momentum of Phonons and the Einstein–de Haas Effect," *Physical Review Letters* 112 (2014): 085503, https://doi.org/10.1103/PhysRevLett.112.085503.

3. L. Zhang and Q. Niu, "Chiral Phonons at High-symmetry Points in Monolayer Hexagonal Lattices," *Physical Review Letters* 115 (2015): 115502, https://doi.org/10.1103/PhysRevLett.115.115502.

4. T. Nova, A. Cartella, A. Cantaluppi, et al., "An Effective Magnetic Field from Optically Driven Phonons," *Nature Physics* 13 (2017): 132–136, https://doi.org/10.1038/nphys3925.

5. M. Hamada, E. Minamitani, M. Hirayama, and S. Murakami, "Phonon Angular Momentum Induced by the Temperature Gradient," *Physical Review Letters* 121 (2018): 175301, https://doi.org/10.1103/PhysRevLett.121.175301.

6. H. Chen, W. Zhang, Q. Niu, and L. Zhang, *Chiral phonons in two-dimensional materials 2D Mater* 6 (2019): 012002.

7. T. Wang, H. Sun, X. Li, and L. Zhang, "Chiral Phonons: Prediction, Verification, and Application," *Nano Letters* 24 (2024): 4311–4318, https://doi.org/10.1021/acs.nanolett.4c00606.

8. D. M. Juraschek and N. A. Spaldin, "Orbital Magnetic Moments of Phonons," *Physical Review Materials* 3 (2019): 064405, https://doi.org/10.1103/PhysRevMaterials.3.064405.

9. S. Coh, "Classification of Materials with Phonon Angular Momentum and Microscopic Origin of Angular Momentum," *Physical Review B* 108 (2023): 134307, https://doi.org/10.1103/PhysRevB.108.134307.

10. D. M. Juraschek, M. Fechner, A. V. Balatsky, and N. A. Spaldin, "Dynamical Multiferroicity," *Physical Review Materials* 1 (2017): 014401, https://doi.org/10.1103/PhysRevMaterials.1.014401.

11. M. Hamada, E. Minamitani, M. Hirayama, and S. Murakami, "Phonon Angular Momentum Induced the Temperature Gradient," *Physical Review Letters* 121 (2018): 175301, https://doi.org/10.1103/PhysRevLett.121.175301.

12. S. F. Maehrlein, I. Radu, P. Maldonado, et al., "Dissecting Spin-phonon Equilibration in Ferrimagnetic Insulators by Ultrafast Lattice Excitation," *Science Advances* 4 (2018): aar5164, https://doi.org/10.1126/sciadv.aar5164.

13. X. Chen, X. Lu, S. Dubey, et al., "Entanglement of Single-photons and Chiral Phonons in Atomically Thin WSe_2," *Nature Physics* 15 (2019): 221–227, https://doi.org/10.1038/s41567-018-0366-7.

14. S. Park and B.-J. Yang, "Phonon Angular Momentum Hall Effect," *Nano Letters* 20 (2020): 7694–7699, https://doi.org/10.1021/acs.nanolett.0c03220.

15. B. Cheng, T. Schumann, Y. Wang, et al., "A Large Effective Phonon Magnetic Moment in a Dirac Semimetal," *Nano Letters* 20 (2020): 5991–5996, https://doi.org/10.1021/acs.nanolett.0c01983.

16. Y. Ren, C. Xiao, D. Saparov, and Q. Niu, "Phonon Magnetic Moment from Electronic Topological Magnetization," *Physical Review Letters* 127 (2021): 186403, https://doi.org/10.1103/PhysRevLett.127.186403.

17. D. M. Juraschek, T. Neuman, and P. Narang, "Giant Effective Magnetic Fields from Optically Driven Chiral Phonons in 4f Paramagnets," *Physical Review Research* 4 (2022): 013129, https://doi.org/10.1103/PhysRevResearch.4.013129.

18. S. R. Tauchert, M. Volkov, D. Ehberger, et al., "Polarized Phonons Carry Angular Momentum in Ultrafast Demagnetization," *Nature* 602 (2022): 73–77, https://doi.org/10.1038/s41586-021-04306-4.

19. H. Chen, W. Wu, J. Zhu, et al., "Chiral Phonon Diode Effect in Chiral Crystals," *Nano Letters* 22 (2022): 1688.

20. S. G. Jeong, J. Kim, A. Seo, et al., "Unconventional Interlayer Exchange Coupling via Chiral Phonons in Synthetic Magnetic Oxide Heterostructures," *Science Advances* 8 (2022): abm4005, https://doi.org/10.1126/sciadv.abm4005.

21. A. Baydin, F. G. G. Hernandez, M. Rodriguez-Vega, et al., "Magnetic Control of Soft Chiral Phonons in PbTe," *Physical Review Letters* 128 (2022): 075901, https://doi.org/10.1103/PhysRevLett.128.075901.

22. H. Ueda, M. Garcıa-Fernandez, S. Agrestini, et al., "Chiral Phonons in Quartz Probed by X-rays," *Nature* 618 (2023): 946.

23. K. Ishito, H. Mao, Y. Kousaka, et al., "Truly Chiral Phonons in α-HgS," *Nature Physics* 19 (2023): 35–39, https://doi.org/10.1038/s41567-022-01790-x.

24. J. Fransson, "Chiral Phonon Induced Spin Polarization," *Physical Review Research* 5 (2023): L022039, https://doi.org/10.1103/PhysRevResearch.5.L022039.

25. J. Luo, T. Lin, J. Zhang, et al., "Large Effective Magnetic Fields from Chiral Phonons in Rare-earth Halides," *Science* 382 (2023): 698–702, https://doi.org/10.1126/science.adi9601.

26. K. Kim, E. Vetter, L. Yan, et al., "Chiral-phonon-activated Spin Seebeck Effect," *Nature Materials* 22 (2023): 322–328, https://doi.org/10.1038/s41563-023-01473-9.

27. F. G. G. Hernandez, A. Baydin, S. Chaudhary, et al., "Observation of Interplay between Phonon Chirality and Electronic Band Topology," *Science Advances* 9 (2023): adj4074, https://doi.org/10.1126/sciadv.adj4074.

28. F. Wu, S. Bao, J. Zhou, et al., "Fluctuation-enhanced Phonon Magnetic Moments in a Polar Antiferromagnet," *Nature Physics* 19 (2023): 1868–1875, https://doi.org/10.1038/s41567-023-02210-4.

29. C. Davies, F. Fennema, A. Tsukamoto, I. Razdolski, A. Kimel, and A. Kirilyuk, "Phononic Switching of Magnetization by the Ultrafast Barnett Effect," *Nature* 628 (2024): 540–544, https://doi.org/10.1038/s41586-024-07200-x.

30. D. Yao and S. Murakami, "Conversion of Chiral Phonons into Magnons in Ferromagnets and Antiferromagnets," *Journal of the Physical Society of Japan* 93 (2024): 034708, https://doi.org/10.7566/JPSJ.93.034708.

31. Q. Wang, M.-Q. Long, and Y.-P. Wang, "Magnetic Moments of Chiral Phonons Induced by Coupling with Magnons," *Physical Review B* 110 (2024): 024423, https://doi.org/10.1103/PhysRevB.110.024423.

32. D. Lujan, J. Choe, S. Chaudhary, et al., "Spin–orbit Exciton–induced Phonon Chirality in a Quantum Magnet," *Proceedings of the National Academy of Sciences* 121 (2024): 2304360121, https://doi.org/10.1073/pnas.2304360121.

33. H. Mustafa, C. Nnokwe, G. Ye, et al., "Origin of Large Effective Phonon Magnetic Moments in Monolayer MoS_2," *ACS Nano* 19 (2025): 11241–11248, https://doi.org/10.1021/acsnano.4c18906.

34. Rückriegel, et al., "Angular Momentum Conservation and Phonon Spin in Magnetic Insulators," *Physical Review B* 101 (2020): 104402, https://doi.org/10.1103/PhysRevB.101.104402.

35. S. Chaudhary, D. M. Juraschek, M. Rodriguez-Vega, and G. A. Fiete, "Giant Effective Magnetic Moments of Chiral Phonons from Orbit-lattice Coupling," *Physical Review B* 110 (2024): 094401, https://doi.org/10.1103/PhysRevB.110.094401.

36. F. Varret, H. Czeskleba, F. Hartmann-Boutron, and P. Imbert, "Étude par Effet Mössbauer De L'ion Fe^{2+} en Symétrie Trigonale dans les Composés du Type $(Fe, M)_2Mo_3O_8$ (M = Mg, Zn, Mn, Co, Ni) et Propriétés Magnétiques de $(Fe, Zn)_2Mo_3O_8$," *Journal de Physique* 33 (1972): 549–564, https://doi.org/10.1051/jphys:01972003305-6054900.

37. P. Strobel and Y. Le Page, "Growth and Morphology of Single Crystals of Hexagonal Molybdates(IV) $M_2Mo_3O_8$ (M = Mn, Fe, Co, Ni)," *Journal of Crystal Growth* 61 (1983): 329–338, https://doi.org/10.1016/0022-0248(83)90370-6.

38. S. Nakayama, R. Nakamura, M. Akaki, D. Akahoshi, and H. Kuwahara, "Ferromagnetic Behavior of $(Fe_{1-y}Zn_y)_2Mo_3O_8$ ($0 \leq y \leq 1$) Induced by Nonmagnetic Zn Substitution," *Journal of the Physical Society of Japan* 80 (2011): 104706, https://doi.org/10.1143/JPSJ.80.104706.

39. Y. Wang, G. L. Pascut, B. Gao, et al., "Unveiling Hidden Ferrimagnetism and Giant Magnetoelectricity in Polar Magnet $Fe_2Mo_3O_8$," *Scientific Reports* 5 (2015): 12268, https://doi.org/10.1038/srep12268.

40. T. Kurumaji, S. Ishiwata, and Y. Tokura, "Doping-Tunable Ferrimagnetic Phase with Large Linear Magnetoelectric Effect in a Polar Magnet $Fe_2Mo_3O_8$," *Physical Review X* 5 (2015): 031034.

41. S. Reschke, A. A. Tsirlin, N. Khan, et al., "Structure, Phonons, and Orbital Degrees of Freedom in $Fe_2Mo_3O_8$," *Physical Review B* 102 (2020): 094307, https://doi.org/10.1103/PhysRevB.102.094307.

42. Y. Chang, Y. Weng, Y. Xie, et al., "Colossal Linear Magnetoelectricity in Polar Magnet $Fe_2Mo_3O_8$," *Physical Review Letters* 131 (2023): 136701, https://doi.org/10.1103/PhysRevLett.131.136701.

43. S. Ghara, E. Barts, K. Vasin, et al., "Magnetization Reversal through an Antiferromagnetic state," *Nature Communications* 14 (2023): 5147, https://doi.org/10.1038/s41467-023-40722-y.

44. T. Ideue, T. Kurumaji, S. Ishiwata, and Y. Tokura, "Giant Thermal Hall Effect in Multiferroics," *Nature Materials* 16 (2017): 797–802, https://doi.org/10.1038/nmat4905.

45. S. Bao, Z.-L. Gu, Y. Shangguan, et al., "Direct Observation of Topological Magnon Polarons in a Multiferroic Material," *Nature Communications* 14 (2023): 6093, https://doi.org/10.1038/s41467-023-41791-9.

46. Z. V. Djordjevic, H. E. Stanley, and A. Margolina, "Site Percolation Threshold for Honeycomb and Square Lattices," *Journal of Physics A: Mathematical and General* 15 (1982): L405–L412, https://doi.org/10.1088/0305-4470/15/8/006.

47. M. Che, J. Liang, Y. Cui, et al., "Magnetic Order Induced Chiral Phonons in a Ferromagnetic Weyl Semimetal," *Physical Review Letters* 134 (2024): 196906.

48. J. Bonini, S. Ren, D. Vanderbilt, M. Stengel, C. E. Dreyer, and S. Coh, "Frequency Splitting of Chiral Phonons from Broken Time-Reversal Symmetry in CrI_3," *Physical Review Letters* 130 (2023): 086701, https://doi.org/10.1103/PhysRevLett.130.086701.

49. F. Wu, J. Zhou, S. Bao, et al., "Magnetic Switching of Phonon Angular Momentum in a Ferrimagnetic Insulator," *Physical Review Letters* 134 (2025): 236701, https://doi.org/10.1103/gcgl-9sbb.

50. S. Bao, J. Liao, Z. Huang, et al., "Magnetic Signature of Chiral Phonons Revealed by Neutron Spectroscopy in Ferrimagnetic $Fe_{1.75}Zn_{0.25}Mo_3O_8$," *Physical Review Letters* 136 (2026): 096502, https://doi.org/10.1103/pq5m-32wj.

51. J. Cui, et al., "Chirality Selective Magnon-phonon Hybridization and Magnon-induced Chiral Phonons in a Layered Zigzag Antiferromagnet," *Nature Communications* 14 (2023): 3396.

52. I. Breslavetz, A. Delhomme, T. Pelini, et al., "Spatially Resolved Optical Spectroscopy in Extreme Environment of Low Temperature, High Magnetic Fields and High Pressure," *Review of Scientific Instruments* 92 (2021): 123909, https://doi.org/10.1063/5.0070934.

53. P. E. Blöchl, "Projector Augmented-wave Method," *Physical Review B* 50 (1994): 17953.

54. G. Kresse and D. Joubert, "From Ultrasoft Pseudopotentials to the Projector Augmented-wave Method," *Physical Review B* 59 (1999): 1758–1775, https://doi.org/10.1103/PhysRevB.59.1758.

55. G. Kresse and J. Furthmüller, "Efficient Iterative Schemes for Ab Initio Total-energy Calculations Using a Plane-wave Basis Set," *Physical Review B* 54 (1996): 11169–11186, https://doi.org/10.1103/PhysRevB.54.11169.

56. J. P. Perdew, K. Burke, and M. Ernzerhof, "Generalized Gradient Approximation Made Simple," *Physical Review Letters* 77 (1996): 3865–3868, https://doi.org/10.1103/PhysRevLett.77.3865.

57. A. Togo, L. Chaput, T. Tadano, and I. Tanaka, "Implementation Strategies in Phonopy and phono3py," *Journal of Physics: Condensed Matter* 35 (2023): 353001, https://doi.org/10.1088/1361-648X/acd831.

58. A. Togo, "First-principles Phonon Calculations with Phonopy and Phono3py," *Journal of the Physical Society of Japan* 92 (2023): 012001, https://doi.org/10.7566/JPSJ.92.012001.

Supporting Information

Additional supporting information can be found online in the Supporting Information section.

Supporting File: adfm75700-sup-0001-SuppMat.docx.